Chemical Engineering Research and Design 192 (2023) 253–267

Available online at www.sciencedirect.com

Chemical Engineering Research and Design

journal homepage: www.elsevier.com/locate/cherd

Map determination for the calculation of dispersion spectra in flowing oil-gas dispersions

Lukas Hafner[a,b,c,*], *Martin Brunner*[c], *Nadja Konrad*[d], *Steffen Schwarzer*[b], *Fadi Dohnal*[a]

[a] *Vorarlberg University of Applied Sciences, Research Center for Microtechnology, Hochschulstraße 1, 6850 Dornbirn, Austria*
[b] *Aalen University, Institute for Drive Technology, Beethovenstraße 1, 73430 Aalen, Germany*
[c] *UMIT TIROL, Institute for Measurement and Sensor Technology, Eduard Wallnöfer-Zentrum 1, 6060 Hall in Tirol, Austria*
[d] *TESTTEC Prüfstandtechnik und Bauteilerprobungs GmbH, Ainet 108, 9951 Ainet, Austria*

ARTICLE INFO

Article history:
Received 18 November 2022
Received in revised form 14 February 2023
Accepted 14 February 2023
Available online 17 February 2023

Keywords:
Static mixer
Bubbles
Dispersions
Aeration
Process simulation
Dimension analysis

ABSTRACT

The production of liquid-gas mixtures with desired properties still places high demands on process technology and is usually realized in bubble columns. The physical calculation models used have individual dimensionless factors which, depending on the application, are only valid for small ranges consisting of flow velocity, nozzle geometry and test setup. An iterative but time-consuming design of such dispersion processes is used in industry for producing a liquid-gas mixture according to desired requirements. In the present investigation, we accelerate the necessary design loops by setting up a physical model, which consists of several subsystems that are enriched by dedicated experiments to realize liquid-gas dispersions with low volume fraction and small air bubble diameters in oil. Our approach allows the extraction of individual dimensionless factors from maps of the introduced subsystems. These maps allow for targeted corrective measures of a production process for keeping the quality. The calculation-based approach avoids the need for performing iterative design loops. Overall, this approach supports the controlled generation of liquid-gas mixtures.

© 2023 The Authors. Published by Elsevier Ltd on behalf of Institution of Chemical Engineers. This is an open access article under the CC BY license (http://creativecommons.org/licenses/by/4.0/).

1. Introduction

The production of liquid-gas mixtures with desired requirements places high demands on process technology and can be found in sectors such as the chemical, plastics, automotive and food industries (Spille et al., 2020; Rama Rao et al., 2007; Hirschberg et al., 2009; Theron and Sauze, 2011; Hafner et al., 2022). In these industries, liquids are interspersed with gases to produce foams and dispersions, metal-gas dispersions, medicines or even foods (Hafner et al., 2022; Bals, 2002; Hafner et al., 2021; Hussein et al., 2014). The manufactured products have requirements about their stiffness, strength and haptics, which must be produced in a targeted, consistent and reproducible manner. These requirements are achieved by the desired gas content, which can be defined by a so-called dispersion spectrum classified by the size of the gas bubbles and their frequency of occurrence. Various scientific studies have already been carried out (Hafner et al., 2022; Bals, 2002; McClure et al., 2016; Rollbusch et al., 2015; Voit et al., 1987; Terasaka et al., 1999;

* Corresponding author at: Vorarlberg University of Applied Sciences, Research Center for Microtechnology, Hochschulstraße 1, 6850 Dornbirn, Austria.
E-mail address: lukas.hafner@hs-aalen.de (L. Hafner).
https://doi.org/10.1016/j.cherd.2023.02.019
0263-8762/© 2023 The Authors. Published by Elsevier Ltd on behalf of Institution of Chemical Engineers. This is an open access article under the CC BY license (http://creativecommons.org/licenses/by/4.0/).

Nomenclature

Symbols used

A	factor for the stokes resistance [–].
B	factor [–].
C_n	factor [n].
D	diameter of the static mixer [m].
d_B	bubble diameter [m].
d_p	pore diameter [m].
d^*	dimensionless bubble diameter [–].
$d(\varphi)$	average bubble diameter after the static mixer [m].
F_A	buoyancy force [N].
F_G	weight force [N].
F_T	inertia force [N].
F_η	viscosity force [N].
F_σ	surface tension force [N].
Fr	Froude number [–].
g	gravitation [ms^{-2}].
h_k	height of the liquid in the oil tank [m].
K	factor [–].
k	factor for the Stokes resistance [–].
K_L	characteristic parameter for a static mixer in laminar conditions [–].
K_P	characteristic parameter for a static mixer [–].
K_T	characteristic parameter for a static mixer in turbulent conditions [–].
L	length [m].
l_{ME}	length of a mixing element [m].
l_{SM}	length of the static mixer [m].
M	mass [m].
m	number of variables [–].
n	number of base units [–].
Re_D	Reynoldsnumber based on the tube inner diameter [–].
T	time [s].
t_{rise}	rise time of a bubble [s].
u	velocity [m s^{-1}].
$u^L_{(a)}$	bubble rise velocity by Levich [m s^{-1}].
$u^{St}_{(a)}$	bubble rise velocity by Stokes [m s^{-1}].
u_∞	bubble rise velocity [m s^{-1}].
$\dot{V}_d$	volume flow of the dispersed phase [m^3s^{-1}].
$\dot{V}_{d\ in}$	dispersed volume flow introduced in the system [m^3s^{-1}].
$\Delta V_{disp\ in}$	initiated volume of the dispersed phase [m^3s^{-1}].
$V_{disp\ out}$	outgassing volume of the dispersed phase [m^3s^{-1}].
$V_{disp\ Tank}$	volume of the dispersed phase in the tank [m^3s^{-1}].
Vi	viscosity number [–].
$\dot{V}_k$	volume flow of the continuous phase [m^3s^{-1}].
V_x	normalized air volume flow [–].
V_y	normalized oil volume flow [–].
V_0	void volume of the static mixer [m^3].
w_b	velocity of the bubble [ms^{-1}].
We	Weber number [–].
w_0	velocity of the gas [ms^{-1}].

Greek letters

Δp_H	pressure drop according to Hirschberg et al. [Pa].
Δp_R	pressure drop according to Rauline et al. [Pa].
Δp_S	pressure drop according to Streiff et al. [Pa].
ε_{Avg}	average energy dissipation rate [W kg^{-1}].
η	dynamic viscosity [$Pa\ s$].
π	variable [–].
ρ_{Fl}	density of the fluid [kgm^3].
ρ_G	density of the gas [kgm^3].
Φ	critical parameter [–].
σ	surface tension [kgs^{-2}].
φ_d	average gas content [–].
$\varphi_{d\ sys}$	dispersed fraction in the total system [–].

Durst and Beer, 1969; Hussein et al., 2017; Shew et al., 2006) for generating, calculating and measuring the sizes of the gas bubbles and their frequency of occurrence.

A physical model is set up in this work for producing a liquid-gas mixture according to desired requirements concerning the gas bubble size and its frequency. The physical model consists of individual and interlinked calculation models. Some of these models possess several dimensionless factors and are known only for a specific viscosity, small flow velocity ranges or a single phase pairing. In the original literature in which the calculation models used were derived, the dimensionless factors were determined iteratively to obtain a correlation between the calculated result and the measurements for exclusively one or a few process points (Hafner et al., 2021; McClure et al., 2016; Rollbusch et al., 2015; Voit et al., 1987; Shew et al., 2006). The interactions of individual changes of a process variable in the corresponding calculation models have not yet been investigated in this manner according to the current state–of-the-art.

To extend the scope of the calculation models and thus to be able to analyse interactions, a characteristic map was created for each dimensionless factor as a function of the dominant process parameters. The results and the established characteristic maps enable a targeted design of bubble columns to produce liquid-gas mixtures. These maps allow for the calculation of the liquid-gas mixture in terms of the gas bubble size and size distribution as a function of the selected process parameters. These maps avoid or reduce iteration loops in the design process and allow for a targeted adjustment of the process parameters in case of deviations from the desired product quality. In this case liquid-gas mixtures with gas contents between 0.2% and 2.2% with average bubble diameters between 170 µm and 200 µm are produced and calculated in a very accurate manner.

2. State of the art

In industry, liquid-gas mixtures are often produced in recirculating systems with a storage tank from which production plants are supplied. The liquid-gas mixtures produced in the storage tanks can be classified by their percentage gas content and the size of the gas bubbles they contain (Bals, 2002; Hafner et al., 2021; Rollbusch et al., 2015; Durst and Beer, 1969). By plotting the gas bubble size and its frequency, a so-called dispersion spectrum can be compiled (Hafner et al., 2021). The dispersion spectrum that occurs in a system depends on the mechanical structure of the system, the physical properties of the liquid and the gas, the phase parameters and the respective process variables. A physical model was set up for generating and regulating the desired dispersions.

The physical model for calculation of the dispersion generation consists of three subsystems. The subsystems are the gas injection (Subsystem 1), the bubble adjustment (Subsystem 2) and a storage tank (Subsystem 3). In the storage tank, the gas content may outgas from the system. If the gas does not outgas fast enough, the liquid-gas mixture circulates through the closed loop, passes Subsystems 1 and 2 and gains additional gas content.

For the prediction of the long-term behaviour of the system, it is necessary to know the size of the gas bubbles. The size of the injected gas bubbles is calculated in Subsystem 1. This size depends significantly on the number, orientation and size of the gas injection points, the dispersion elements as well as the phase parameters (Hafner et al., 2022; Bals, 2002; Hafner et al., 2021; McClure et al., 2016; Durst and Beer, 1969). Subsequently, the gas bubbles are broken up in Subsystem 2. A static mixer, as commonly used with different geometries in industry and science (Spille et al., 2020; Hirschberg et al., 2009; Theron and Sauze, 2011), is implemented to adjust the gas bubbles to a desired size and size distribution. The degree of comminution depends largely on the size of the gas bubbles in front of the static mixer and the speed at which the gas bubbles are conveyed through the static mixer as well as the geometry of the static mixer (Rama Rao et al., 2007; Hirschberg et al., 2009; Theron and Sauze, 2011). Subsystem 3 is a storage tank into which the liquid-gas mixture is transported. The quantity of gas in the storage tank is determined by the rising speed of the gas bubbles contained in the liquid-gas mixture and by the distance the gas bubbles need to rise before outgassing at the surface. For this purpose, it is necessary to know the size of the gas bubbles in the storage tank and the quantity of gas that is continuously fed into or outgas for each gas bubble size (Voit et al., 1987; Shew et al., 2006; Clift et al., 1978; Koebe, 2004; Peebles and Garber, 1953).

The mutual interaction between these three subsystems determines the gas concentration in the storage tank, i.e. the saturation limit of the liquid-gas mixture at constant process conditions as well as the achievable bubble size distribution. The derivation of the subsystems is described in detail below.

2.1. *Subsystem 1: Injection of a targeted gas bubble size*

Various studies have already been carried out which, among other things, have investigated the influence of different nozzle geometries and arrangements, phase pairings and the orientations of the components involved on the gas bubble diameters injected into liquids (Hafner et al., 2022; Bals, 2002; Hafner et al., 2021; Rollbusch et al., 2015; Voit et al., 1987; Durst and Beer, 1969; Fainerman and Miller, 2004). In this context, Kumar and Kuloor (Kumar and Kuloor, 1970) divided the process of bubble formation into a two-stage process, distinguishing between the so-called expansion and the detachment phase. During the expansion phase, the forming gas bubble is constantly connected to the nozzle, the dispersion element, and fills with inflowing gas as it increases its size. The forces acting on a forming gas bubble are shown in Fig. 1. The forces include the Buoyancy force F_A, the weight force F_G, the viscosity force F_η, the inertia force F_T and the surface tension force F_σ. The magnitude and direction of the forces shown is time-dependent and, therefore, dependent on the current expansion phase. The forces are divided into stabilizing and destabilizing forces. By increasing the gas bubble diameter, the ratio of these forces changes. If the destabilizing forces become larger than the stabilizing forces,

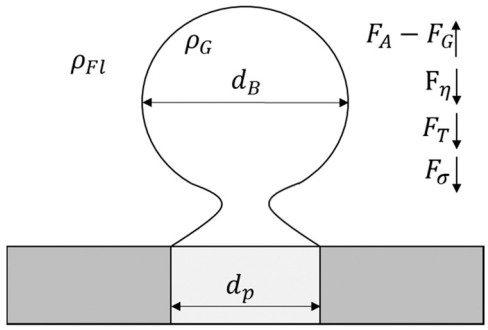

Fig. 1 – Forces acting on a forming gas bubble at an upward directed nozzle.
Based on Hafner et al. (2021).

the gas bubble begins to rise. As the bubble rises, a so-called gas bubble tube is formed through which the gas bubble is filled even further during its rise. As the gas bubble fills, its Buoyancy force increases and the gas bubble accelerates in the direction of this force, while the gas bubble tube gains length but loses diameter. Finally, the gas bubble tube separates from the dispersion element and the gas bubble formed can rise as a function of the acting frictional, viscous and upward forces (Kumar and Kuloor, 1970).

Two bubble formation mechanisms exist as depicted in Fig. 2: the bubble gassing and the jet gassing (Bals, 2002; Brauer, 1971). Theses mechanisms are separated by a transition zone. Different threshold values are mentioned in the literature, for example (Bals, 2002; Brauer, 1971) state a Weber number of 1,3. The Weber number compares the destabilizing inertial force acting on an gas bubble with the stabilizing surface tension during a relative motion of the gas bubble.

Brauer as well as Bothe and Schlüter have defined the transition on the basis of the critical parameter Φ (Brauer, 1971; Bothe and Schlüter, 2013; Bothe et al., 2017). Whereby, depending on the media combination used, it must be investigated for which value of the critical parameter Φ the transition occurs (Hafner et al., 2021). The following parameters were identified so far for predicting the transition

$$\Phi = 1 + \sqrt{\frac{We^2}{Fr}},\ We = \frac{w_0^2 d_B \rho_G}{\sigma},\ Fr = \frac{w_b^2 \rho_{Fl}}{(\rho_{Fl} - \rho_G) g d_B}. \tag{1}$$

Bothe et al (Bothe et al., 2017). defined the dimensionless gas bubble diameter

$$d^* = \frac{d_b}{\sqrt[3]{\frac{3\sigma d_p}{\rho_{Fl} g}}} \tag{2}$$

for a media-independent comparability of the bubble sizes.

2.2. *Subsystem 2: Calculation of gas bubble sizes according to the static mixer*

The gas bubbles introduced into the system are passed through a static mixer (Subsystem 2) where they are split up depending on the acting forces. The use of static mixers can be found in many areas of industry. They are required in the cosmetics industry, food industry, plastics industry as well as in many other industries where uniformly mixed media combinations or also broken up particles such as drops or bubbles in flows must be produced. Depending on the application, the static mixers are used for mixing liquid-liquid, solid-liquid and liquid-gas mixtures (Spille et al., 2020; Rama

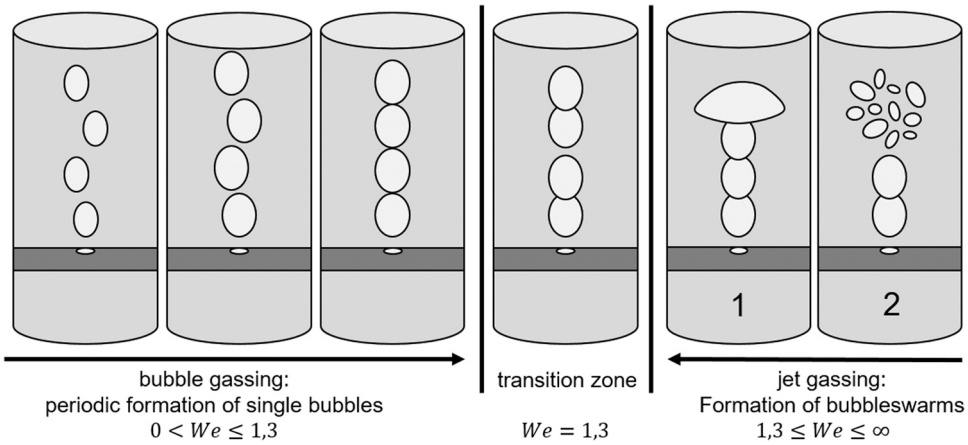

Fig. 2 – Difference between bubble gassing and jet gassing and the transition area. Based on Hafner et al. (2021).

Rao et al., 2007; Hirschberg et al., 2009; Theron and Sauze, 2011). The so-called mixing quality of different media indicates how evenly the mixed media are distributed across the cross-section of the flow. The so-called dispersion spectrum, the bubble size distribution, indicates how large the particles are after comminution by the static mixer. The mixing quality as well as the particle size after the static mixer depend on the geometry and the process conditions. The geometry is determined by the type of static mixer, the installation position as well as the dimensioning and the number of individual mixing elements. There are different types of static mixers that differ in their geometry and thus in the mixing quality. In the work carried out here, a Sulzer SMX-plus mixer with a diameter of 25 mm is used.

An SMX-plus mixer element consists of several crossed rods arranged at an angle of 45° to the tube axis, see Fig. 3 on the right. Depending on the diameter of the tube used, the number of crossed rods varies. A static mixer of length l_{SM} consists of several mixer elements of length l_{ME} twisted by 90° in the axial direction, which are firmly connected to each other, see Fig. 3 on the left. The number of mixer elements arranged in series is increased in order to achieve a better mixing quality and to be able to generate smaller bubbles. This increases the hydraulic resistance of the flow at this point, which leads to a measurable pressure drop between the inlet and the outlet of the static mixer. This pressure drop is sometimes used as a reference for the mixing quality of the static mixer. The pressure drop has been estimated in the literature for different types of static mixers and different media combinations (Hirschberg et al., 2009; Theron and Sauze, 2011; Al Taweel et al., 2013; Lobry et al., 2011). Hirschberg et al. (2009) investigated which geometry changes reduce the pressure drop without reducing the mixing quality. They calculated the specific pressure drop across the static mixer as a function of the factor K_L, the length L_{SM} and the diameter D. K_L depends on the number of crossed bars of the static mixer. The pressure drop Δp_H according to Hirschberg is calculated as

$$\Delta p_H = \frac{K_L \rho u^2 L_{SM}}{Re_D D} \tag{3}$$

Rama Rao et al. (2007) reviewed the pressure drop calculations in the literature. Rauline et al. (1998) calculated the pressure drop of the static mixer using the factor K_P as a function of dynamic viscosity η and velocity u

$$\Delta p_R = \frac{K_P \eta u L_{SM}}{D^2} \tag{4}$$

Streiff et al. (1999) proposed an expression that combines the contributions of the turbulent (K_T) and laminar flow (K_L)

$$\Delta p_S = \frac{u^2 L_{SM}}{D}\left(\frac{K_L}{Re_D} + K_T\right), \tag{5}$$

which covers a larger range of static mixers. In all definitions, the amount of factors used to adjust the K_L, K_p or K_L and K_T factor depends on the geometry of the static mixer as well as the pipe into which the mixer is placed.

Finally, to calculate the particle size after the static mixer, the calculation of the dissipated energy is necessary. This can be calculated by the pressure loss over the length of the

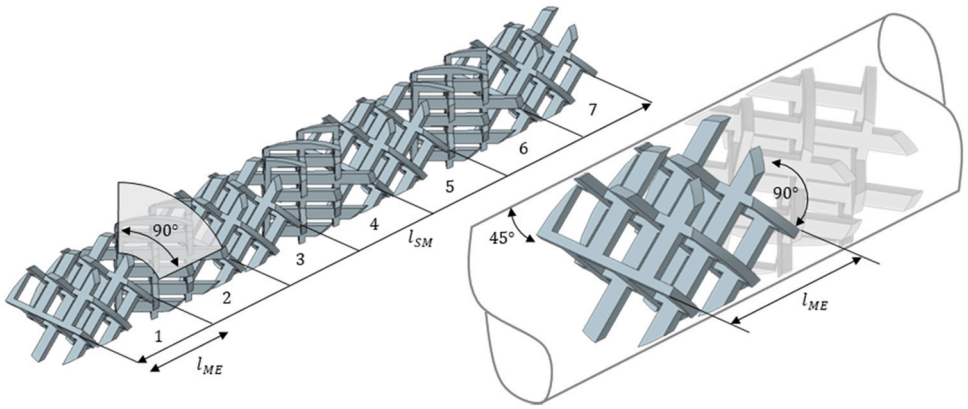

Fig. 3 – Illustration of a static mixer type SMX-plus of the company Sulzer.

static mixer. The dissipated energy represents the energy available to enable mixing or comminution of the media used Al Taweel et al. (2013) has calculated the dissipated energy rate as a function of the length of the static mixer as follows.

$$\varepsilon_{Avg} = \frac{u\Delta p}{\rho L_{SM}} \tag{6}$$

Theron and Sauze (2011) compared different calculation models of static mixers for the comminution of gas bubbles. A dimensional analysis according to Buckingham's Pi Theorem identified which of the presented calculation models is physically plausible and has therefore the potential of being applied in a broadband physical model. This methodology helps defining dimensionless parameters without knowing the physical equation. In this way m dimensioned quantities transform into $m - n$ dimensionless quantities. Here, n is the number of SI-based units used to compose the m basic quantities. When performing the Pi Theorem, it is critical to guess all the quantities involved in the physical problem. Missed quantities may lead to plausible results but are usually not valid for the general case. The calculation model established by Theron and Sauze (2011); Streiff et al. (1999) for calculating the particle size after a static mixer in SMV, SMX and SMXL design is shown in the present paper. Hirschberg et al. (2009) extended this calculation for turbulent flows of an oil-water-mixture for the geometry of the SMX-plus mixer and described as applicable by a comparison with tests (Hirschberg et al., 2009; Theron and Sauze, 2011). According to (Streiff et al., 1999), the basic variables that influence the particle size after the static mixer are the surface tension σ, the mass-specific energy dissipation rate ε, the density ρ and the gas content φ_d. The particle diameter after the static mixer is calculated as

$$d(\varphi) = C_n(1 + k\varphi_d)\left(\frac{(1 + BV_i)We_c}{2}\right)^{0,6}\left(\frac{\sigma}{\rho_c}\right)^{0,6}\left(\frac{\rho_c}{\rho_d}\right)^{0,1}\varepsilon_{Avg}^{-0,4}. \tag{7}$$

This calculation rule consists of the basic units mass, length and time ($n = 3$). The dimensions of all variables in Eq. (7) are listed in Table 1:

With regard to Table 1, the particle diameter can be described by the following function:

$$d_B = f(Cn, k, \varphi, B, V_i, We, \sigma, \rho_c, \rho_d, \varepsilon_{Avg}) \tag{8}$$

The number of variables is $m = 11$ and the number of base units is $n = 3$. According to the Pi Theorem, the relation in Eq. (8) can be rewritten by by $m - n = 8$ dimensionless quantities (Wang et al., 2016; Zohuri, 2017). Selecting σ, ρ, $\varepsilon_{Avg}$and d_B as independent variables yields

$$\begin{aligned} \dim \sigma &= M^{x_1}L^{y_1}T^{z_1} = M^1L^2T^{-2} \\ \mathrm{im}\ \rho &= M^{x_2}L^{y_2}T^{z_2} = M^1L^{-3}T^0 \\ \dim \varepsilon_{Avg} &= M^{x_3}L^{y_3}T^{z_3} = M^0L^{-3}T^2 \end{aligned} \tag{9}$$

The determinant of the exponents confirms that the variables are indeed independent,

$$\begin{vmatrix} x_1 & y_1 & z_1 \\ x_2 & y_2 & z_2 \\ x_3 & y_3 & z_3 \end{vmatrix} = \begin{vmatrix} 1 & 2 & -2 \\ 1 & -3 & 0 \\ 0 & -3 & 2 \end{vmatrix} = -4 \neq 0. \tag{10}$$

Assuming a product approach

$$1 = \sigma^x\varepsilon_{Avg}^y\rho^z d_B^{-1}, \tag{11}$$

and the underlying basic dimensions M (mass), T (time) and L (length) of the chosen variables gives

Table 1 – Dimensions of variables in Eq. (7).

	Cn	k	φ	B	Vi	We	σ	ρ_c	ρ_d	ε_{Avg}	d_B
M	0	0	0	0	0	0	1	1	1	0	0
L	0	0	0	0	2	0	2	-3	-3	-3	1
T	0	0	0	0	-1	0	-2	0	0	2	0

$$1 = \left(\frac{M^1}{T^2}\right)^x\left(\frac{M^2}{T^3}\right)^y\left(\frac{M^1}{L^3}\right)^z. \tag{12}$$

The unknown exponents must hold the relations

$$x = -z,\ y = \frac{3}{2}z,\ x = -\frac{2}{3}y. \tag{13}$$

This set of equations possesses multiple solutions. We are looking for a solution with the lowest values for the exponents. One solution is

$$x = 0.6,\ y = -0.4,\ z = -0.6. \tag{14}$$

From Eqs.(11) and (14), the basic equation

$$\pi = d_B^{-1}\sigma^{0.6}\varepsilon_{Avg}^{-0.4}\rho^{-0.6} \tag{15}$$

is established. A comparison of the dimensional analysis in Eq. (15) with the calculation model established by Streiff et al. in Eq. (7) reveals that the very same exponents occur. This supports the usefulness of the prediction in Eq. (7) and the dimensionless factors used therein.

Further non-applicable attempts have been made by choosing independent variables as

$$\pi^m = \sigma^x\varepsilon_{Avg}^y\rho_c^z = L^{2y-3z}M^{x+y}T^{-2x-3y} \tag{16}$$

and

$$\pi^n = \sigma^x\varepsilon_{Avg}^y d_B^z = L^{2y+z}M^xT^{-2x-3y} \tag{17}$$

where both Eq. (16) and eq. (17) have a dependency of the used variables proven by a determinant of the exponents equal to zero.

Experimental tests are carried out in the following for a validation of the finding in Eq. (15).

The calculation of Streiff et al. in Eq. (7) includes physical variables and process-specific dimensionless factors, which have been iteratively adapted to experiments in literature (Theron and Sauze, 2011; Streiff et al., 1999). These include the factors C_n, k and B, for which values were determined for different media combinations and flow regimes. The factor V_i is the viscosity number and represents the influence of the viscosity of the dispersed phase on the dispersion. Due to the direct correlation between the viscosity number V_i and the factor$B$, the two factors are treated as the single factor BV_i in the following. We_c is the critical Weber number. All factors C_n, k and BV_i are therefore variables and change with variations of the process. For example, the viscosity of the mixture changes with a varying proportion of the disperse phase, which subsequently changes the critical Weber number and also the dissipation energy of the static mixer (Hirschberg et al., 2009; Lobry et al., 2011; Streiff et al., 1999). The factors C_n, k and BV_i are constant at fixed process parameters $\dot{V}_d$, $\dot{V}_k$and T. The dependency of these process-dependent factors on the process parameters $\dot{V}_d$, $\dot{V}_k$and T are described as $C_n(\dot{V}_d, \dot{V}_k, T)$, $k(\dot{V}_d, \dot{V}_k, T)$ and $BV_i(\dot{V}_d, \dot{V}_k, T)$. This dependency has not been investigated in the literature so far.

The other factors φ_d, $\varphi_{d_{Sys}}$ and V_0 can be adapted to the existing situation with respect to media combination, flow regime, mixer geometry and temperature (Hu et al., 2020).

The factor φ_d is the fraction of the dispersed phase in the static mixer and is determined by the dispersed fraction in the total system $\varphi_{d_{Sys}}$ and the additional volume of the dispersed phase introduced into the system as well as the void volume of the static mixer V_0,

$$\varphi_d(t) = \frac{\varphi_{d_{Sys}}(t) + \dot{V}_{din}}{V_0 u} \tag{18}$$

Depending on the size of the gas bubbles in the system, their ascent rate changes and thus also the saturation limit of the overall system.

2.3. *Subsystem 3: Calculation of gas bubble rise velocity*

The gas bubble rise velocity in liquids has already been dealt with in various scientific papers. The difference in densities between the mixed phases has a major influence. The rise velocity is described by Stokes' law for Reynolds numbers with Re ≤ 1.4 and gas bubble diameters with a diameter $d_B \leq 2$mm as follows (Koebe, 2004).

$$u_{(a)}^{St} = \frac{1}{18}\frac{g(\rho_L - \rho_G)}{\eta_L}d_B^2 \tag{19}$$

In comparison, Levich (Koebe, 2004) assumed a boundary layer flow around the rising bubble, which leads to a reduction of the Stokes resistance by a factor of two leading to

$$u_{(a)}^{L} = \frac{1}{36}\frac{g(\rho_L - \rho_G)}{\eta_L}d_B^2 \tag{20}$$

Further iterative correlations of the drag coefficient have been performed by other researchers based on these calculations. For example, Clift et al., Peebles and Garber (Clift et al., 1978; Koebe, 2004; Peebles and Garber, 1953) found that the rate of ascent changesdepending on the magnitude of the forces acting on the bubble surface. This effect can be captured best by adjusting the Stokes resistance. According to Talaia (2007) the Pi Theorem for the calculation of the bubble rise velocity for single bubbles in a bubble column was carried out and its parameters adapted to experiments of the media combination air and glycerine. The basic relation was established for the rise velocity of a single bubble in a liquid

$$u_\infty = k\frac{g(\rho_L - \rho_G)}{\eta_L}d_B^2 \tag{21}$$

was established for the rise velocity of a single bubble in a liquid (Koebe, 2004). All of the above calculation models represent the sub-areas of an overall system that are used to calculate the dispersion that occurs with an gas bubble size. These were combined in the present work in a comprehensive calculation model and its parameters adjusted to measurement data from a test rig.

3. Materials and methods

The materials, the structure of the test rig used, the structure of the physical model and the tests carried out are described below. In particular, the procedure and methodology for adapting the calculation models used are discussed.

3.1. *Testrig*

To produce and measure a desired dispersion for automotive hydraulics test purposes, a test rig was set up that can aerate liquid with compressed air. In automotive hydraulics applications, oil-air dispersions with air volume fractions of up to 5% with a very precisely defined average air bubble size are required for testing transmissions and pumps in order to perform acoustic adjustments, efficiency analyses and other investigations. The test rig contains of an oil tank with a capacity of 100 l. Two separate circuits, the aeration circuit (A) and the measuring circuit (B) are fed from the oil tank. The measuring circuit is implemented for measuring the dispersion spectrum in the storage tank and avoiding coalescence or dissipation effects caused by flow-induced pressure gradients in the aeration circuit. The two circuits as well as the storage tank are shown in Fig. 4.

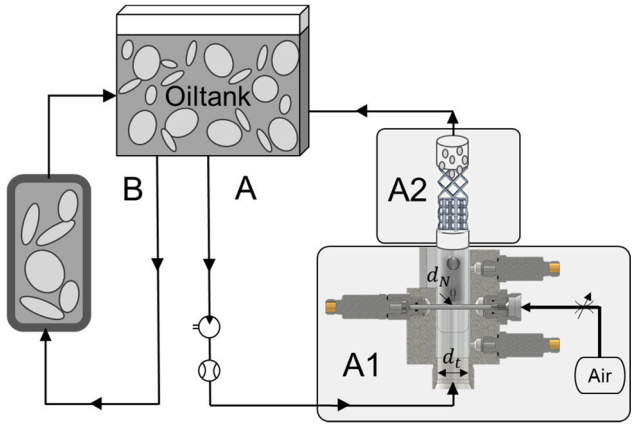

Fig. 4 – The test rig with separate circuits: (A) aeration circuit, (B) measurement circuit.

The aeration circuit is fed by a controlled volume flow from the oil tank. A gas injection point is located in the aeration circuit (see A1 in Fig. 4). The gas injection point consists of a steel cylinder inserted at right angle to the direction of flow, on which a hole with a diameter of $d_N = 0.2$mmis drilled centrally in the flow direction. A regulated compressed air supply is connected to the steel cylinder, through which a regulated air volume flow is introduced into the liquid flow at a desired pressure. The pressure is measured by pressure sensors directly within the steel cylinder and upstream or downstream of the steel cylinder within the liquid stream. The diameter of the pipe conveying liquid is $d_t = 27$mm, the diameter of the steel cylinder introduced transversely to the flow is 4mm. The pumped liquid is oil, the introduced gas is air.

A Sulzer SMX-plus static mixer (see A2 in Fig. 4) is introduced vertically in flow direction from the steel cylinder to adjust the gas bubbles already present in the stream and the newly introduced air bubbles. After the oil-air mixture has been conveyed through the static mixer, it enters the oil tank again from where the aeration circuit (see A in Fig. 4) is fed again.

The measuring circuit (B) is operated at a constant volume flow from the tank. A specially developed optical measuring system is installed in the measuring circuit, which measures the dispersion in the storage tank with regard to the dispersion spectrum it contains. The measuring system consists of a sight glass through which the foamed oil is conveyed. The sight glass consists of two plane-parallel glass plates with a plate spacing below 1 mm. The aerated oil is captured by an industrial camera and its recordings are evaluated by a specially developed evaluation algorithm in which gas bubble sizes of different sizes and shapes are classified, counted and evaluated by a multi-stage procedure as seen in

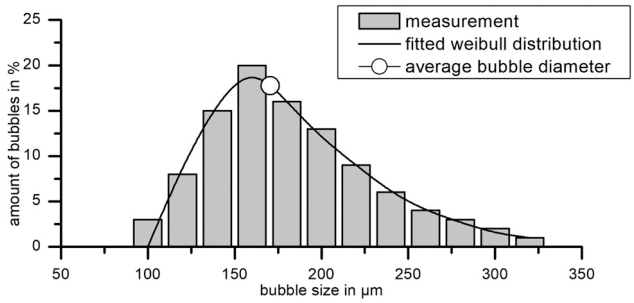

Fig. 5 – Measured and evaluated data by the evaluation algorithm of the Smart Bubble System.

Fig. 5. The contours of the bubbles are detected and then equivalent circular diameter is calculated.

3.2. *The physical model*

To create a physical model, the previously presented calculation models were linked in dependence on each other. The linking of the subsystem was carried out using Matlab/Simulink. In the model created, the phase parameters density and viscosity are output variables and defined as a function of temperature and ambient pressure. The process parameters oil flow rate, air flow rate and temperature are input variables and can be varied as desired. The phases used have the following physical characteristics: Table 2.

In the model set up, the gas bubble size at the outlet of the static mixer is calculated. The size of the gas bubbles created there is the input variable for calculating the average gas content in the storage tank. The gas saturation limit for the storage tank reaches its maximum when the volume of the disperse phase $V_{disp_{in}}$ fed into the storage tank equals the volume of the disperse phase $V_{disp_{out}}$ outgassing from the storage tank at time t by

$$V_{disp_{out}}(t) = V_{disp_{in}}(t). \tag{22}$$

The outgassing volume of the disperse phase $V_{disp_{out}}$ at time t is calculated by the volume of the disperse phase $V_{disp_{Tank}}$ currently contained in the storage tank at the respective time t and the necessary rise time t_{rise} of an gas bubble with the diameter d_B to the surface of the continuous phase by

$$V_{disp_{out}}(t) = \frac{V_{disp_{Tank}}(t)}{t_{rise}(d_B)}. \tag{23}$$

The time required for a gas bubble to rise to the surface of the continuous phase,

$$t_{rise}(d_B) = \frac{u_{(a)}}{h_k(\varphi_d)} \tag{24}$$

depends on the gas bubble rise velocity $u_{(a)}$ and level h_k of the storage tank. The level height in turn varies with a changing gas saturation φ_d of the supply tank.

As has been shown in many research papers, the rate at which a single bubble rises varies with the phase properties surrounding it (Shew et al., 2006; Clift et al., 1978; Koebe, 2004; Peebles and Garber, 1953; John et al., 2006). The factor describing the surface forces acting on the gas bubble and the change of the velocity gradient at the gas bubble surface is, as shown before, the Stokes resistance (Shew et al., 2006). Since the forces acting on the surface of the gas bubble change with changing gas saturation and a variation in gas bubble sizes, the Stokes resistance is replaced by a variable that is determined iteratively depending on the selected process factors. The correlation

$$u_{(a)}(\dot{V}_d, \dot{V}_k, T) = A(\dot{V}_d, \dot{V}_k, T)\frac{g(\rho_L - \rho_G)}{\eta_L}d_B^2 \tag{25}$$

follows for the rise speed of the gas bubble by using a process-specific factor $A(\dot{V}_d, \dot{V}_k, T)$ for the Stokes resistance according to Eq. (22).

In the set up model 4 dimensionless factors occur that influence the saturation limit, as well as the size of the gas bubbles introduced into the system. Among them are the factors Cn, k, BVi, which describe the behaviour of the static mixer and the factor A, which represents the Stokes resistance of a rising gas bubble in the oil. For the factor k, a value depending on the type of static mixer is chosen in different reports. For the following calculations, the factor $k = 1000$ is chosen analogous to the assumptions of Theron and Sauze (2011). Further, it has been presented in scientific works that the factors Cn, A, BVi change with changing phase properties (Spille et al., 2020; Hirschberg et al., 2009; Voit et al., 1987; Terasaka et al., 1999; Shew et al., 2006; Clift et al., 1978; Koebe, 2004; Peebles and Garber, 1953; Al Taweel et al., 2013; Lobry et al., 2011; John et al., 2006). Therefore experiments were performed to be able to adjust the dimensionless factors as needed.

Table 2 – Characteristic parameters of the phases used.

	density $\rho_{15°C}$ *in* kgm^{-3}	*dyn. viscosity* $\eta_{dyn15°}$ *in* $kgm^{-1}s^{-1}$	*kin. viscosity* $\nu_{kin15°}$ *in* kgs^{-2}
oil	870	0.072	$83.04 \cdot 10^{-6}$
air	1.225	$1.84 \cdot 10^{-5}$	$1.53 \cdot 10^{-5}$

All the tests and calculations presented in this paper are carried out with an oil temperature of 40 °C.

3.3. *Tests performed*

The tests performed were carried out with the test rig set up. Each measuring point is recorded after a run-in period of 10 min. All measurement points shown are calculated mean values over a measurement period of one minute with a frame rate of 0.2 Hz. The experiments were repeated 10 times to ensure that the experiments are repeatable and the results are consistent. The maximum deviation of the measurement results of the mean air content is 0.8% with the mean deviation between measurements being 0.1%. The maximum deviation of the measurement results of the mean gas bubble diameter is 1.2% with the mean deviation being 1.0%.

The presented tests differ with regard to the volume flow of the pumped oil and the volume flow of the introduced air. The tests carried out with results are shown in Fig. 5. The preserved oil volume flow varied between 100 l/min (0.04 m/s) and 180 l/min (0.07 m/s). The preserved air volume flow varied between 0.1 l/min (0.005 m/s) and 0.4 l/min (0.021 m/s).

The tests carried out produced average air contents between 0.2% and 2.2%, see Fig. 6 left, and average gas bubble diameters between 170 µm and 200 µm, see Fig. 6 right. With an increasing air flow rate, an increase in the percentage air content can be observed at a constant oil flow rate, see Fig. 6 left. By increasing the oil flow rate pumped, a decreasing gas bubble size in the system can be observed from an oil flow rate of 140 l/min. To enable calculation of the percentage air content and the average gas bubble diameter, the factors Cn, BV_i and A shown can be determined as a function of the measurement results.

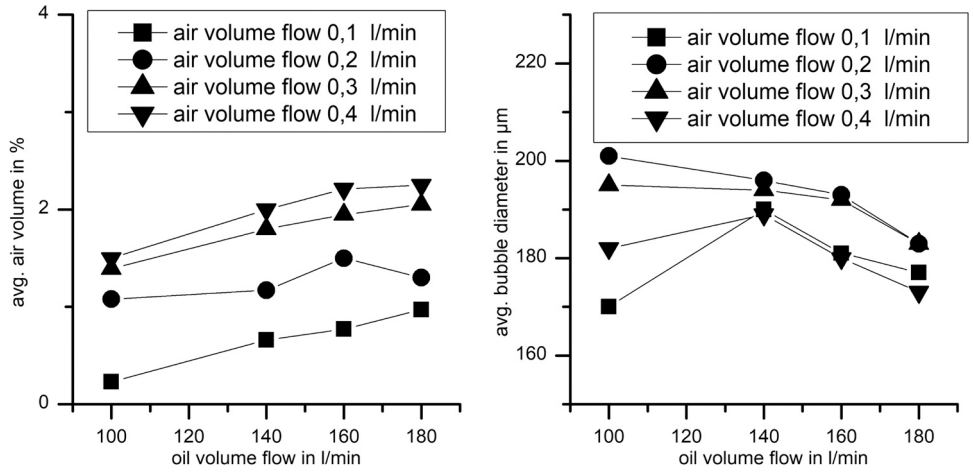

Fig. 6 – representation of the tests carried out on the test rig.

4. Adaptation of the physical models

To define the scope of the physical model, the previously presented dimensionless factors Cn, BV_i and A can be iteratively adapted to the generated measurement results. Following this, characteristic diagrams can be developed from the factors, which describe the instantaneous value of the respective factor as a function of the process parameters oil flow rate and air flow rate. In the following, two different methods, creation of polynomials and interpolation, are compared.

4.1. *Polynomial approximation*

An iterative adjustment of the factors Cn, BV_i and A, was performed using the Response Optimizer Toolbox from Matlab. The factors are adjusted to the generated measurement results at a maximum deviation of 2% on the target percentage air content and mean gas bubble diameter. The calculated results with an exact adjustment of the factors by the polynomial approximation are shown in Fig. 7 and Fig. 8 with unfilled symbols the measurements with filled symbols.

Fig. 7 compares the results of the measurement of the mean gas bubble diameter on the test rig with the generated calculated results. As an input condition for the optimization of the dimensionless factors Cn, BV_i and A a maximum deviation of 1.5% is specified. The average deviation between the measurements and the calculated results is 1.3%, with the maximum deviation occurring at 1.5% for an air flow rate of $\dot{V}_d = 0.1\frac{l}{min}$ and an oil flow rate of $\dot{V}_k = 180\frac{l}{min}$.

Fig. 8 compares the average air content evaluated during the measurements with the calculated results. The average deviation between the measurements and the calculated results is 0.1%, with a maximum deviation of 0.2% for an air flow rate of $\dot{V}_d = 0.1\frac{l}{min}$ and an oil flow rate of $\dot{V}_k = 100\frac{l}{min}$.

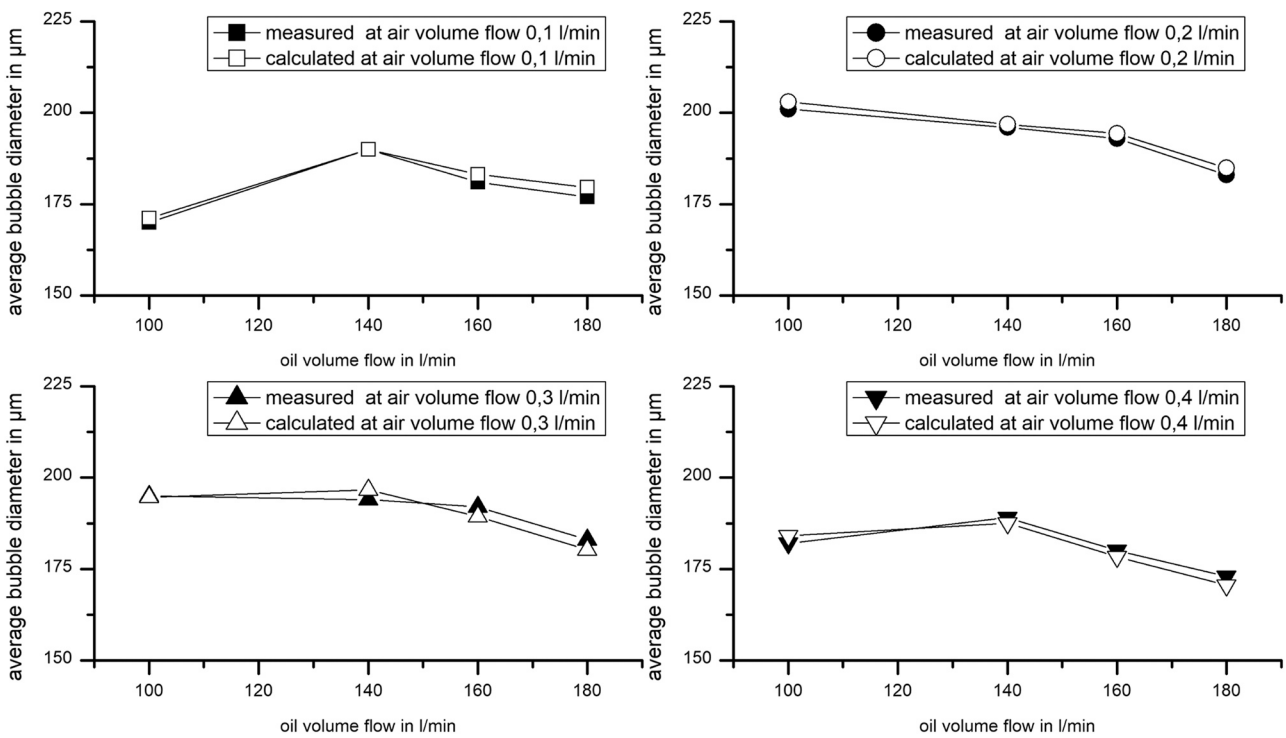

Fig. 7 – comparison of the measurement results and the calculated results of the average gas bubble diameter after exact adjustment of the factors Cn, BVi, and A.

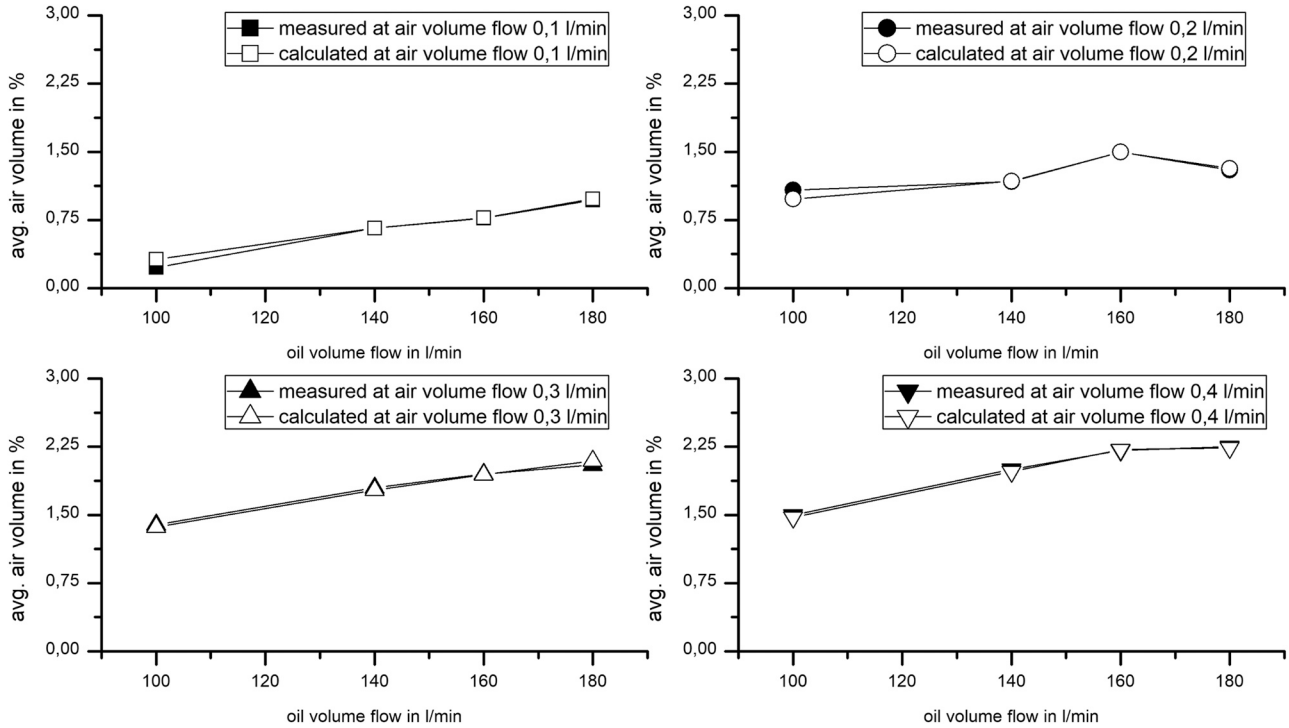

Fig. 8 – comparison of the measurement results and the calculated results of the average air content after exact adjustment of the factors Cn, BVi and A.

Table 3 – iteratively determined values for the factor Cn.

		air volume flow			
		0.1l/min	0.2l/min	0.3l/min	0.4l/min
oil volume flow	100l/min	0.02649	0.04027	0.03048	0.02470
	140l/min	0.01698	0.03447	0.02304	0.01935
	160l/min	0.01372	0.02129	0.02083	0.01452
	180l/min	0.01293	0.02807	0.01949	0.01653

In the calculations performed, values for the factors Cn, BV_i und A are iteratively determined.

Values between 0.01293 and 0.04027 were determined for Cn. The values determined for Cn are listed in Table 3.

Values between 0.0001 and 12 were determined for BV_i. Between an air flow rate of 0.2 l/min and 0.3 l/min, a local minimum occurs. The iteratively determined values for BV_i are listed in Table 4.

In addition to the factors Cn und BV_i the values for factor A were also determined. These are listed in Table 5. For factor A values between 0.03382 and 0.1105 were determined. These lie between the values given in the literature for the Stokes drag coefficient for small single bubbles according to Koebe, Peebles et al. and Clift et al (Clift et al., 1978; Koebe, 2004; Peebles and Garber, 1953).

Table 4 – iteratively determined values for the factor BVi.

		air volume flow			
		0.1l/min	0.2l/min	0.3l/min	0.4l/min
oil volume flow	100l/min	12.00000	0.22520	0.16340	0.24010
	140l/min	7.50900	0.19340	0.11830	0.19990
	160l/min	7.69200	0.67390	0.11840	0.51860
	180l/min	5.26000	0.12620	0.00010	0.01415

In order to adapt the factors Cn, BV_i and A a mathematical model is adapted.

Different curve fitting methods were performed including a polynomial fit and a interpolation method to specify the dimensionless factors Cn, BV_i and A. In the following those methods are shown.

For verification purposes, the results are compared with verification tests.

4.2. *Curvefitting*

The first method to adjust the dimensionless factors as needed is by designing polynomials. The dimensionless factors Cn, BV_i and $A$are converted into second- and third-degree polynomials, depending on their gradient behaviour. The definition range of the generated polynomials is defined here for an oil volume flow between $100\frac{1}{\text{min}} \leq \dot{V}_k \leq 180\frac{1}{\text{min}}$ and for the air volume flow $0.1\frac{1}{\text{min}} \leq \dot{V}_d \leq 0.4\frac{1}{\text{min}}$. In the calculation, the oil and air volume flow is normalized by

$$V_x = \frac{\dot{V}_d - 0.25}{0.1155} \tag{26}$$

and

$$V_y = \frac{\dot{V}_k - 145}{30.55}. \tag{27}$$

A third-degree polynomial can be determined for the factor Cn as a function of the oil and air volume flow. The polynomial for the factor Cn is calculated by

$$\begin{aligned} Cn(V_{x,y}) = {} & 27.34\cdot10^{-3} - 9.695\cdot10^{-3}V_x - 11.04\cdot10^{-3}V_y + 6.06\cdot10^{-3}V_x^2 \\ & + 0.73\cdot10^{-3}V_xV_y + 2.815\cdot10^{-5}V_y^2 + 6.143\cdot10^{-3}V_x^3 + 0.42V_x^2V_y \\ & - 0.2049\cdot10^{-3}V_xV_y^2 + 4.057\cdot10^{-3}V_y^3 \end{aligned} \tag{28}$$

where BV_i follows as a third degree polynomial as,

Table 5 – iteratively determined values for the stokes resistance coefficient A.

		air volume flow			
		0.1l/min	0.2l/min	0.3l/min	0.4l/min
oil volume flow	100l/min	0.051320	0.051560	0.073230	0.110500
	140l/min	0.033820	0.051750	0.066130	0.084440
	160l/min	0.036170	0.046100	0.063310	0.087420
	180l/min	0.034390	0.055070	0.069060	0.095270

$$BV_i(V_{x,y}) = -0.3043 - 0.2474V_x - 0.1445V_y - 2.651V_x^2 - 0.7601V_xV_y + 0.01021V_y^2 - 1.862V_x^3 - 0.8113V_x^2V_y - 0.1435V_xV_y^2 \quad (29)$$

and the factor A as a third degree polynomial by,

$$A(V_{x,y}) = 0.05391 + 0.01711V_x + 0.2606 \cdot 10^{-3}V_y + 4.76 \cdot 10^{-3}V_x^2 + 0.5724 \cdot 10^{-3}V_xV_y + 5.47 \cdot 10^{-3}V_y^2 + 1.295 \cdot 10^{-3}V_x^3 - 3.672 \cdot 10^{-3}V_xV_y^2 + 1.025 \cdot 10^{-3}V_y^3. \quad (30)$$

By transferring the dimensionless factors Cn, BV_i and A to the physical model, the models can be compared with the tests carried out on the test rig. A comparison between measurements and calculations is shown in Fig. 9 and Fig. 10.

Fig. 9 compares the results of the physical model with the measurements of the mean air content. In this case, the physical model calculates the dimensionless factors Cn, BV_i and A by Eqs. (26) to (30) shown previously as a function of the process factors $\dot{V}_d$ and $\dot{V}_k$. The top left shows the results with an air flow rate of $\dot{V}_d = 0.1\frac{l}{min}$, the top right shows the results with an air flow rate of $\dot{V}_d = 0.2\frac{l}{min}$, the bottom left shows the results with an air flow rate of $\dot{V}_d = 0.3\frac{l}{min}$, and the bottom right shows the results with an air flow rate of $\dot{V}_d = 0.4\frac{l}{min}$. In each of the four diagrams, the measurements on the test bench are shown with filled symbols the results of the physical model are shown with the not filled symbols.

The average deviation between the calculated results and the measurements is 0.17%. The largest deviation between calculations and measurement occurs for an air volume flow of $\dot{V}_d = 0.3\frac{l}{min}$ and an oil volume flow of $\dot{V}_k = 100\frac{l}{min}$. Here, the maximum deviation between measurement and calculated result is 0.63%, see Fig. 8 bottom left.

Fig. 10 shows a comparison of the results of the mean gas bubble diameters generated on the test rig with the calculations of the physical model. Analogous to Fig. 9, the physical model calculates the dimensionless factors Cn, BV_i and A from Eqs. (26) to (30). The representation as well as the arrangement is carried out analogously to Fig. 9.

A mean deviation of 2.3% with a maximum deviation of 11.3% occurs between all measurements and calculated results shown in Fig. 10. The maximum deviation occurs for an air volume flow of $\dot{V}_d = 0.3\frac{l}{min}$ and an oil volume flow of $\dot{V}_k = 100\frac{l}{min}$, see Fig. 10 bottom left.

The second adaption method for the dimensionless factors Cn, BV_i and A is a interpolation between iteratively determined values. In the following the mean and maximum deviation between the measurements and the physical model are investigated.

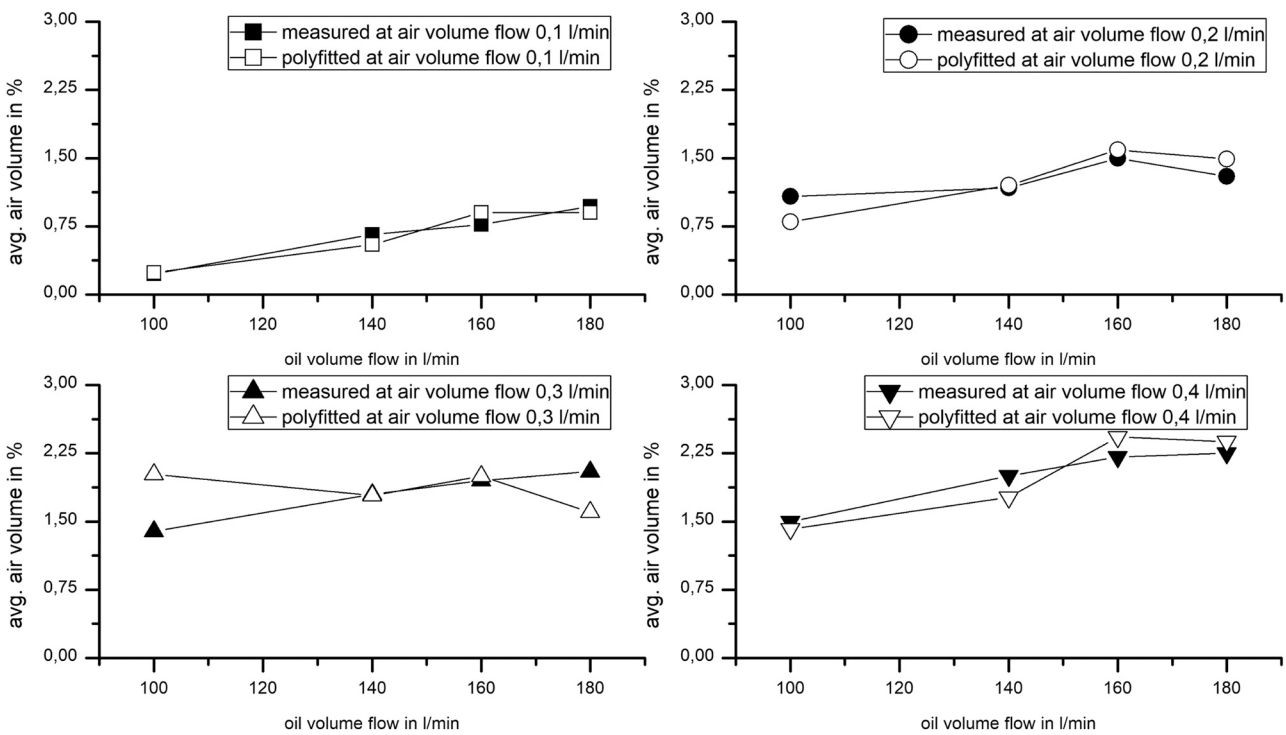

Fig. 9 – illustration of the created measurements of the average air content on the test rig and the physical model adjusted by polynomials.

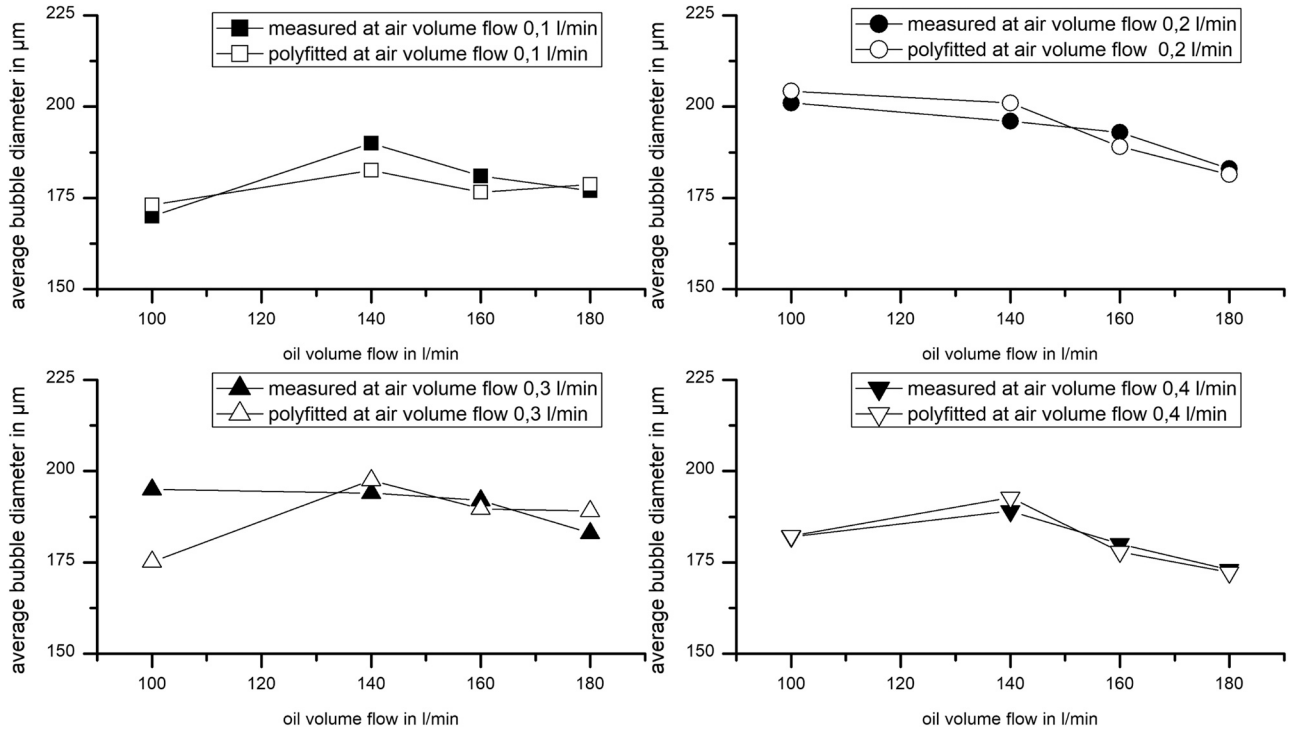

Fig. 10 – presentation of the created measurements of the average gas bubble diameters on the test rig and the physical model adjusted by polynomials.

Fig. 11 and Fig. 12 show the measurement and the calculated results by an interpolation dimensionless factors Cn, BV_i and A from Table 3–5. The representation of the symbols as well as the arrangement of the diagrams is performed analogously to Fig. 9. Fig. 11 shows the comparison of the average air content between the measurements and the physical model. Over all measurement points in Fig. 11, an average deviation of 0.02% and a maximum deviation of 0.1% between the calculated result and the measurement results.

Fig. 12 shows a comparison between the measurement results of the mean gas bubble diameters on the test rig and the physical model. Over all measurements, the average deviation is 0.9%, with a maximum deviation of 1.5%.

Further, the intermediate process points are examined to investigate whether there is a physical relationship between the dimensionless factors Cn, BV_i and A. If the maps generated here can be determined both by an interpolation and by the polynomials set up at the intermediate process points in

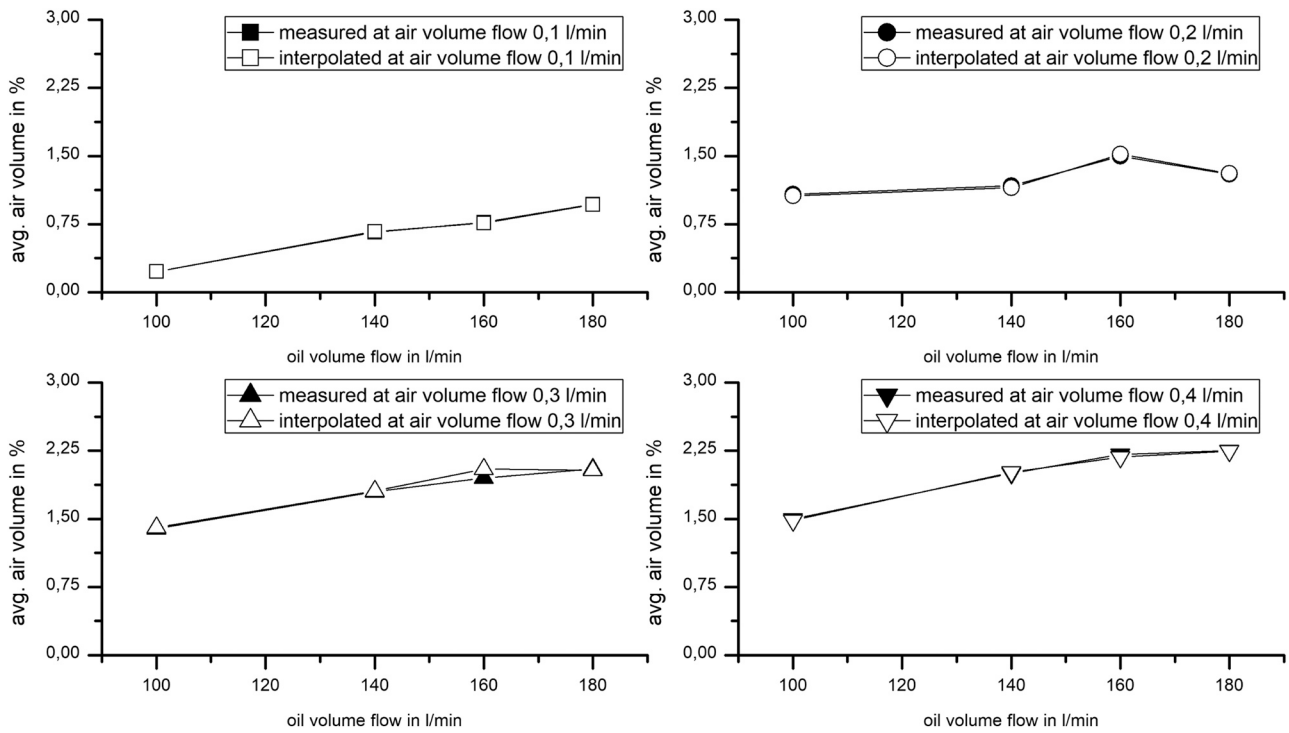

Fig. 11 – presentation of the created measurements of the average air content on the test rig and the physical model adjusted by interpolation.

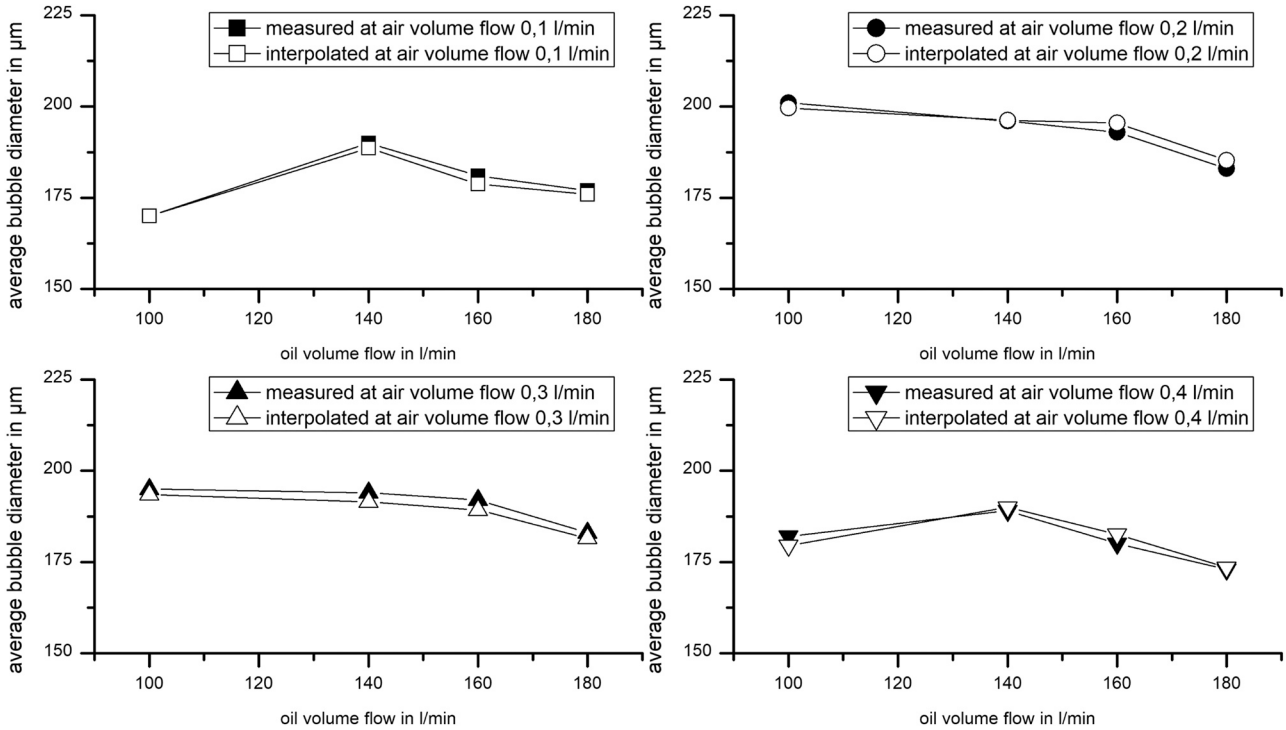

Fig. 12 – representation of the created measurements of the average gas bubble diameters on the test rig and the physical model adjusted by interpolation.

such a way that small deviations arise between the measurements performed and the physical model, this methodology can be considered to achieve the desired results. The results of this investigation are listed below.

5. Results

As shown in Fig. 9 to Fig. 12, a correlation between the measurements and the physical model is recognized. For the calculation of the average air content, by fitting the dimensionless factors by polynomials, maximum deviations of 0.6% arise from the measurements performed, see Fig. 9. For an interpolation between the dimensionless factors, between the calculations and the measurements of the percent air content, a mean deviation of 0.02% arises, see Fig. 11. Between the measurement and the calculation of the mean gas bubble diameters, by a polynomial fitting of the dimensionless factors, a maximum deviation of 11.5% arises, see Fig. 10 bottom left. For an interpolation between the dimensionless factors, a maximum deviation of 1.5% arises between the measurements and the calculations of the introduced mean gas bubble diameters, see Fig. 11.

In addition, the determined characteristic maps of the dimensionless factors Cn, BV_i and A are used to calculate the intermediate process points for model validation, which is a common procedure for model validation (Bäßler et al., 2022a, 2022b). The results are shown in Fig. 13 and Fig. 14.

Fig. 13 shows the measurements of the average air content on the test rig and the calculation results generated with the physical model at the intermediate process points. The measurements are shown with filled symbols, the calculated results by interpolations with unfilled symbols and the calculated results by polynomials with unfilled and crossed-out symbols. The diagrams with respect to the constant air flow rate are arranged as in Fig. 9 to Fig. 12.

For the measurement points of the mean air content, the polynomials show mean deviations of 0.15% between the measurements and the calculated results. For an interpolation between the intermediate points of the iteratively determined maps, a mean deviation of 0.02% arises.

Fig. 14 shows a comparison between the measurements of the mean gas bubble diameter made on the test rig and the results calculated with the different physical models. The data points are labelled in the same way as in Fig. 13.

For an adjustment of the factors Cn, BV_i and A by polynomials, average deviations of 1.9% arise between the measurements and the results of the physical model. The maximum deviation between the measurements performed and the results of the physical modelling is 5.6%. The maximum deviation occurs for an air flow rate of $\dot{V}_d = 0{,}4\frac{l}{min}$ and an oil flow rate of $\dot{V}_k = 120\frac{l}{min}$, see Fig. 14, bottom right.

For the factor adjustment performed with an interpolation, an average deviation of 1.2% occurs, with the maximum deviation between measurement and physical model being 2.2%. The maximum deviation between measurement and calculation occurs for an air flow rate of $\dot{V}_d = 0{,}1\frac{l}{min}$ and an oil flow rate of $\dot{V}_k = 120\frac{l}{min}$, see Fig. 14 top left.

The intermediate points shown were verified by means of measurements carried out on the test rig. The measurements were carried out analogously to the previously presented measurements. Table 6.

A summary of all results obtained during the investigation is given in Table 3. It compares the average and maximum deviation of the results calculated by interpolation and polynomial fitting from the measurements on the test rig.

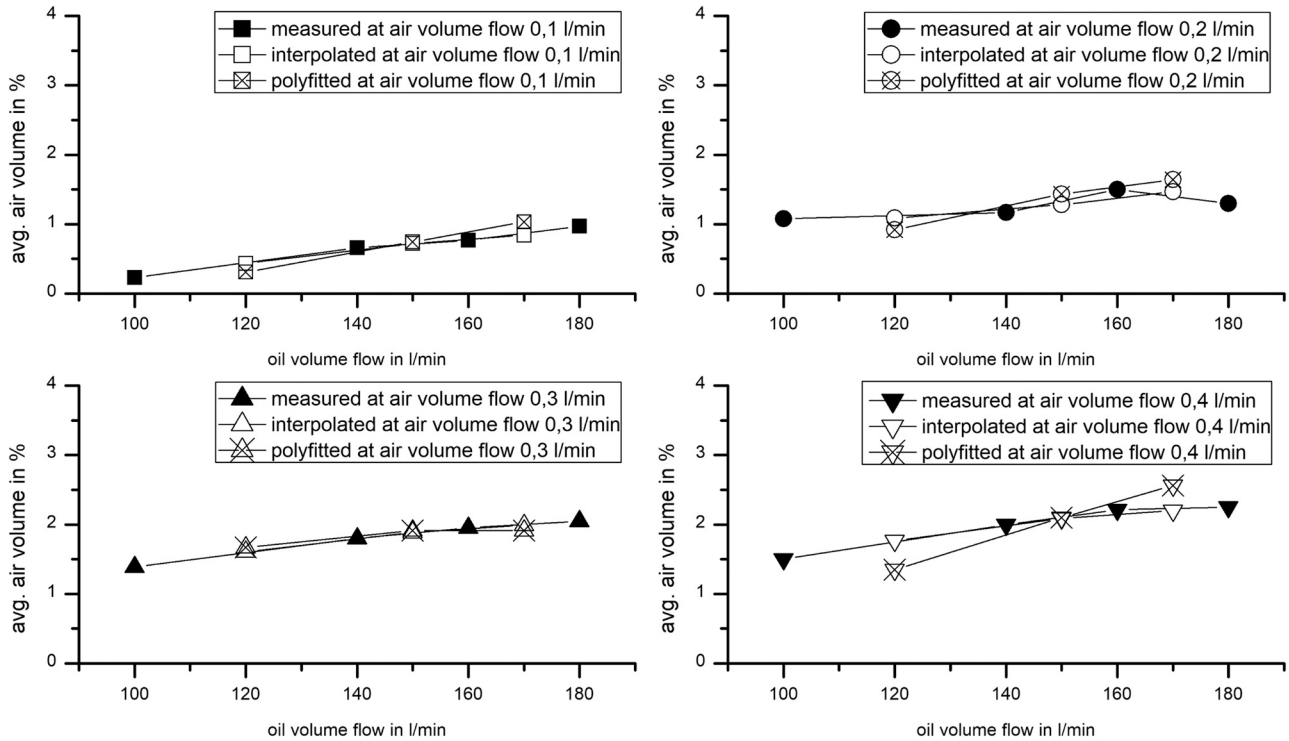

Fig. 13 – presentation of the created measurements of the average air content at the test rig and the physical model created by interpolation as well as by polynomial fitting at the intermediate process points.

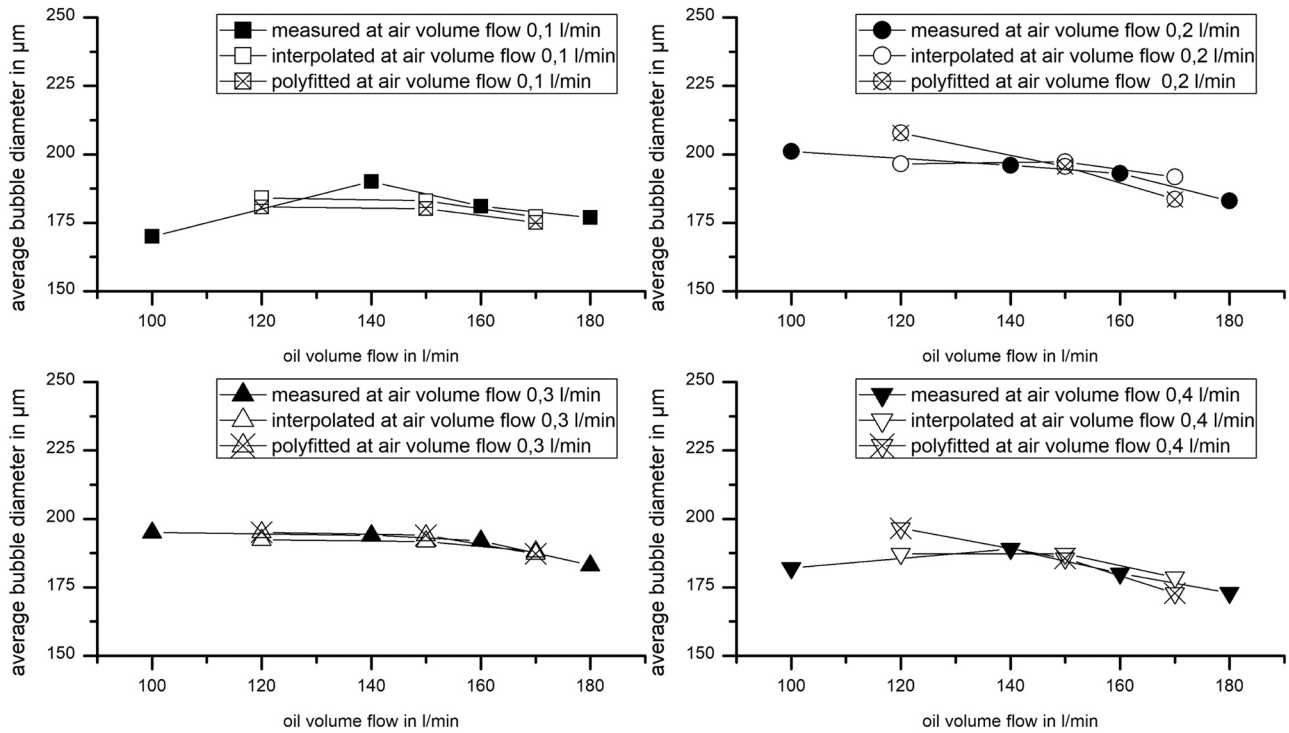

Fig. 14 – representation of the created measurements of the average gas bubble diameters at the test rig and the physical model created by interpolation as well as by polynomial fitting at the intermediate process points.

Table 6 – summary of all the results obtained during the tests carried out.

	interpolation		interpolation intermed. points		polynomials		polynomials intermed. points	
	avg.%	avg.∅	avg.%	avg.∅	avg.%	avg.∅	avg.%	avg.∅
avg. dev. in %	0.02	0.9	0.02	1.2	0.2	2.3	0.2	1.9
max. dev. in %	0.1	1.5	0.07	2.2	0.6	11.3	0.4	5.6

6. Conclusion

In the presented work, two different methods of a map determination and implementation for the formation of a physical model of a dispersion spectrum are compared with each other. The calculations are benchmarked against measurement. The dispersion spectrum in the performed work is given by the percentage air content and the mean gas bubble diameter. In the calculations performed by the physical model, a specific determination of the characteristic diagram enables a calculation of the dispersion spectrum for considerably larger flow velocity ranges than is possible so far according to the current state of the technology.

The characteristic diagram is implemented in a physical model by employing two different methods. An interpolation method and a polynomial fit of individual physical factors on the basis of process corner points.

The model calculations highlight the benefit of the proposed method. On the one hand, it enables a targeted design of dispersion processes, whereby iterative design loops can be reduced. On the other hand, a desired disperison spectrum can be easily changed by adjusting the process factors, which was not possible with the prior art.

The validity of the presented model can be related to the range of tests performed and presented. How far the validity of the model can be extended must be checked by further investigations. These include different geometries, media combinations, arrangements and temperature es.

Declaration of Competing Interest

The authors declare the following financial interests/personal relationships which may be considered as potential competing interests: Lukas Hafner reports financial support was provided by Federal Ministry for Economy and Energy. Martin Brunner reports financial support was provided by Austrian Research Promotion Agency. Fadi Dohnal reports financial support was provided by Austrian Research Promotion Agency. Nadja Konrad reports was provided by Austrian Research Promotion Agency. Steffen Schwarzer reports was provided by Federal Ministry for Economy and Energy.

Acknowledgement

The authors acknowledge for the project Smart Bubble System, the technical support by testtec Prüfstands- und Bauteilerprobungs GmbH in Austria and the financial support within European program IraSME (ZIM: project number ZF4113820, FFG project number 877671).

References

Spille, C., Hu, X., Maiwald, M.I., Herzog, D., Hoffmann, M., Emmelmann, C., Smirnova, I., Schlüter, M., 2020. SMART reactors: intelligente additiv gefertigte strukturierte einbauten zur optimierung von gas/flüssig-reaktionen. Chem. Ing. Tech. 92 (9), 1328. https://doi.org/10.1002/cite.202055194

Rama Rao, N.V., Baird, M., Hrymak, A.N., Wood, P.E., 2007. Dispersion of high-viscosity liquid–liquid systems by flow through SMX static mixer elements. Chem. Eng. Sci. 62 (23), 6885–6896. https://doi.org/10.1016/j.ces.2007.08.070

Hirschberg, S., Koubek, R., Moser, F., Schöck, J., 2009. An improvement of the Sulzer SMX™ static mixer significantly reducing the pressure drop. Chem. Eng. Res. Des. 87 (4), 524–532. https://doi.org/10.1016/j.cherd.2008.12.021

Theron, F., Sauze, N.Le, 2011. Comparison between three static mixers for emulsification in turbulent flow. Int. J. Multiph. Flow. 37 (5), 488–500. https://doi.org/10.1016/j.ijmultiphaseflow.2011.01.004

Hafner, L., Bäßler, R., Schwarzer, S., Kley, M., Dohnal, F., 2022. Bubble size detection by process ancillaries. Chem. Ing. Tech. 94 (8), 1096–1104. https://doi.org/10.1002/cite.202100175

Bals, A., 2002. Grundlagen der blasenbildung an einzelporen und lochplatten. Chem. Ing. Tech. 74, 337–344.

Hafner, L., Schwarzer, S., Dohnal, F., 2021. Creation of liquid-air dispersions in oil and water: comparison of calculations and measurements. Chem. Ing. Tech. 93 (10), 1629–1635. https://doi.org/10.1002/cite.202100023

Hussein, W., Khan, M.S., Zamorano, J., Espic, F., Yoma, N.B., 2014. A novel ultrasound based technique for classifying gas bubble sizes in liquids. Meas. Sci. Technol. 25 (12), 125302. https://doi.org/10.1088/0957-0233/25/12/125302

McClure, D.D., Wang, C., Kavanagh, J.M., Fletcher, D.F., Barton, G.W., 2016. Experimental investigation into the impact of sparger design on bubble columns at high superficial velocities. Chem. Eng. Res. Des. 106, 205–213. https://doi.org/10.1016/j.cherd.2015.12.027

Rollbusch, P., Bothe, M., Becker, M., Ludwig, M., Grünewald, M., Schlüter, M., Franke, R., 2015. Bubble columns operated under industrially relevant conditions – Current understanding of design parameters. Chem. Eng. Sci. 126, 660–678. https://doi.org/10.1016/j.ces.2014.11.061

Voit, H., Zeppenfeld, R., Mersmann, A., 1987. Calculation of primary bubble volume in gravitational and centrifugal fields. Chem. Eng. Technol. 10, 99–103.

Terasaka, K., Tsuge, H., Matsue, H., 1999. Can. J. Chem. Eng. (Can. J. Chem. Eng.) 77, 458–464.

Durst, F., Beer, H., 1969. Blasenbildung an düsen bei gasdispersionen in flüssigkeiten. Chem. Ing. Tech. 18, 1000–1006.

Hussein, W.B., Essmat, S.A., Yoma, N., 2017. On bubble sizing in water by ultrasound. Int. J. Interact. Mob. Technol. 11 (2), 128. https://doi.org/10.3991/ijim.v11i2.6590

Shew, W.L., Poncet, S., Pinton, J.-F., 2006. Force measurements on rising bubbles. J. Fluid Mech. 569, 51. https://doi.org/10.1017/S0022112006002928

Clift, R., Grace, J.R., Weber, M.E., 1978. Bubbles, Drops, and Particles, second ed. Dover Pubn Inc.

Koebe M., *Numerische Simulation aufsteigender Blasen mit und ohne Stoffaustausch mittels der Volume of Fluid (VOF) Methode* 2004.

Peebles, F.N., Garber, H.J., 1953. Chem. Eng. Prog. 49 (2), 88–99.

Fainerman, V.B., Miller, R., 2004. Maximum bubble pressure tensiometry–an analysis of experimental constraints. Adv. Colloid Interface Sci. 108–109, 287–301. https://doi.org/10.1016/j.cis.2003.10.010

Kumar, R., Kuloor, N.K., 1970. Advances in chemical engineering. 8, 255–368.

Brauer H., 1971. Grundlagen der Einphasen- und Mehrphasenströmungen: Grundlagen der chemischen Technik - Verfahrenstechnik der chemischen und verwandter Industrien, Sauerländer, Aarau und Frankfurt am Main.

Bothe, M., Schlüter, M., 2013. Modellierungsparameter für Blasenströmungen. Chem. Ing. Tech. 85 (7), 1023–1035. https://doi.org/10.1002/cite.201300051

Bothe, M., Christlieb, M.-A., Hoffmann, M., Tedjasukmana, O., Michaux, F., Rollbusch, P., Becker, M., Schlüter, M., 2017. Can. J. Chem. Eng. (Can. J. Chem. Eng.) 95 (5), 902–912. https://doi.org/10.1002/cjce.22759

Al Taweel, A.M., Azizi, F., Sirijeerachai, G., 2013. Static mixers: effective means for intensifying mass transfer limited reactions. Chem. Eng. Process.: Process.Intensif. 72, 51–62. https://doi.org/10.1016/j.cep.2013.08.009

Lobry, E., Theron, F., Gourdon, C., Le Sauze, N., Xuereb, C., Lasuye, T., 2011. Turbulent liquid–liquid dispersion in SMV static mixer at high dispersed phase concentration. Chem. Eng. Sci. 66 (23), 5762–5774. https://doi.org/10.1016/j.ces.2011.06.073

Rauline, D., Tanguy, P., le Blévec, J.-M., Bousquet, J., 1998. Numerical investigation of the performance of several static mixers. Can. J. Chem. Eng. 76 (76), 527–535.
Streiff F.A., Jaffer S., Schneider G., Proceedings of the 3rd International Symposium on Mixing in Industrial Processes 1999, 107 – 144.
Wang, D., Liu, Y., Zhang, Z., Shao, P., Zhang, T., 2016. Math. Probl. Eng. 2016, 1–8. https://doi.org/10.1155/2016/4170371
Zohuri, B., 2017. Dimensional Analysis Beyond the Pi Theorem. Springer International Publishing, Cham.
Hu, X., Spille, C., Schlüter, M., Smirnova, I., 2020. Smart structures—additive manufacturing of stimuli-responsive hydrogels for adaptive packings. Ind. Eng. Chem. Res. 59 (43), 19458–19464. https://doi.org/10.1021/acs.iecr.0c03137
Talaia, M., 2007. Eng. Technol. 264–268. https://doi.org/10.5281/zenodo.1070173
John, S., Schlüter, M., Scheid, S., Parchmann, H., Räbiger, N., 2006. Eine methode zur berechnung der relativgeschwindigkeit von gasblasen in dreiphasenströmungen – teil 2: praxisrelevante gasgehalte. Chem. Ing. Tech. 78 (1–2), 64–72. https://doi.org/10.1002/cite.200500101
Bäßler, R., Bäßler, T., Kley, M., 2022a. Classification of load and rotational speed at wire-race bearings using convolutional neural networks with vibration spectrograms. TM Tech. Mess. 89 (5), 352–362. https://doi.org/10.1515/teme-2021-0143
Bäßler, T., Bäßler, R., Kley, M., 2022b. Augmented mel-spectrogram VGG-16 model for axial and radial load classification at wire-race bearings. TM Tech. Mess. 89 (9), 573–579. https://doi.org/10.1515/teme-2022-0039